

Wideband near-infrared emission from $GaScO_3:Cr^{3+}$ phosphors with a perovskite structure

Chong Li(李翀), Mengyu Zhang(张梦宇), Chuancheng Zhang(张传成), Wenzhi Su(宿文志), Yong Zou(邹勇), Shoujun Ding(丁守军), and Qingli Zhang(张庆礼)

Citation: Chin. Phys. B, 2025, 34 (**8**): 087502. DOI: 10.1088/1674-1056/add506
http://cpb.iphy.ac.cn; http://iopscience.iop.org/cpb

What follows is a list of articles you may be interested in

Distance-dependent magnetization modulation induced by inter-superatomic interactions in Cr-doped $Au_6Te_{12}Se_8$ dimers

Yurou Guan(官雨柔), Nanshu Liu(刘南舒), Cong Wang(王聪), Fei Pang(庞斐), Zhihai Cheng(程志海), and Wei Ji(季威)

Chin. Phys. B, 2024, 33 (**12**): 127502. DOI: 10.1088/1674-1056/ad8625

Band engineering of valleytronics WSe_2–MoS_2 heterostructures via stacking form, magnetic moment and thickness

Yanwei Wu(吴彦玮), Zongyuan Zhang(张宗源), Liang Ma(马亮), Tao Liu(刘涛), Ning Hao(郝宁), Wengang Lü(吕文刚), Mingsheng Long(龙明生), and Lei Shan(单磊)

Chin. Phys. B, 2023, 32 (**10**): 107506. DOI: 10.1088/1674-1056/acb761

Spin correlations in the *S=1* armchair chain Ni_2NbBO_6 as seen from NMR

Kai-Yue Zeng(曾凯悦), Long Ma(马龙), Long-Meng Xu(徐龙猛), Zhao-Ming Tian(田召明), Lang-Sheng Ling(凌浪生), and Li Pi(皮雳)

Chin. Phys. B, 2021, 30 (**4**): 047503. DOI: 10.1088/1674-1056/abc2b5

Gd impurity effect on the magnetic and electronic properties of hexagonal Sr ferrites: A case study by DFT

Masomeh Taghipour, Mohammad Yousefi, Reza Fazaeli, Masoud Darvishganji

Chin. Phys. B, 2020, 29 (**7**): 077505. DOI: 10.1088/1674-1056/ab8d9f

Thickness-dependent magnetic order and phase transition in V_5S_8

Rui-Zi Zhang(张瑞梓), Yu-Yang Zhang(张余洋), Shi-Xuan Du(杜世萱)

Chin. Phys. B, 2020, 29 (**7**): 077504. DOI: 10.1088/1674-1056/ab8db1

Wideband near-infrared emission from $GaScO_3$:Cr^{3+} phosphors with a perovskite structure

Chong Li(李翀)[1], Mengyu Zhang(张梦宇)[1], Chuancheng Zhang(张传成)[1], Wenzhi Su(宿文志)[1], Yong Zou(邹勇)[1], Shoujun Ding(丁守军)[1,2,†], and Qingli Zhang(张庆礼)[3]

[1] *School of Microelectronics and Data Science, Anhui University of Technology, Maanshan* 243002, *China*
[2] *Anhui Provincial Joint Key Laboratory of Disciplines for Industrial Big Data Analysis and Intelligent Decision, Maanshan* 243002, *China*
[2] *Anhui Institute of Optics and Fine Mechanics, Chinese Academy of Sciences, Hefei* 230031, *China*

(Received 21 March 2025; revised manuscript received 28 April 2025; accepted manuscript online 7 May 2025)

Cr^{3+}-activated phosphors have attracted significant attention for their tunable emission, spanning narrow-band red to broadband near-infrared (NIR) luminescence, depending on the crystal field environment. Here, we report the realization of wideband NIR emission in Cr^{3+}-doped $GaScO_3$ ($GaScO_3$:Cr^{3+}) phosphors with perovskite structure. The phosphors were synthesized by traditional solid-state reaction method. The first-principles calculations were conducted and the results demonstrate that the octahedral [GaO_6] sites exhibit relatively weak crystal field strength ($Dq/B \approx 2.2$), facilitating efficient spin-allowed transitions of Cr^{3+} from the $^4T_2$ state to the $^4A_2$ state. The photoluminescence spectroscopy revealed an exceptionally broad NIR emission band from a range of 700 nm–1200 nm with full width at half maximum (FWHM) of 145 nm under 465-nm excitation. Overall, these results highlight the viability of $GaScO_3$:Cr^{3+} as a highly promising material for wideband NIR applications.

Keywords: $GaScO_3$, perovskite phosphors, Cr^{3+}-doped, near-infrared emission, density functional theory

PACS: 75.20.En, 61.72.–y, 76.30.Fc, 78.55.–m, 71.15.Mb

DOI: 10.1088/1674-1056/add506 **CSTR:** 32038.14.CPB.add506

1. Introduction

The development of broadband near-infrared (NIR) light sources has garnered substantial attention owing to their extensive applications in night vision, nondestructive testing, and information encryption.[1–6] Therefore, the research on high-performance NIR broadband phosphors has garnered significant attention.[7,8] Currently, research on NIR phosphors primarily concentrates on two aspects: (i) using transition metals as activator, such as Cr^{3+}, Ni^{2+}, Mn^{3+}, to offering broad 3d–3d transitions, (ii) using rare-earth ions as activator, such as Pr^{3+}, Nd^{3+}, Tm^{3+}, and Yb^{3+}, to exhibit characteristic 4f–4f lines.[9–14] However, transition metal Ni^{2+}-activated phosphors remain limited by severe thermal quenching and low absorption cross-sections. Besides, rare-earth systems are constrained by their narrow excitation bands and weak absorption intensities.[15–17] Compared with them, Cr^{3+} ions in weak-field octahedral sites ($Dq/B < 2.3$) demonstrate broadband NIR emission (650 nm–1300 nm) through spin-allowed $^4T_2 \rightarrow {}^4A_2$ transitions, with the emission maximum and bandwidth being highly sensitive to crystal field strength. This tunability stems from the strong coupling of the $3d^3$ electronic configuration with the ligand field, enabling emission peak modulation over 100 nm through host lattice engineering. Consequently, Cr^{3+} has emerged as an ideal candidate for NIR emission centers.[18–20]

It has been reported that ScF_3:Cr^{3+} ($\lambda_{max} = 853$ nm, FWHM = 140 nm),[21] $Sr_{0.92}Mg_{0.91}Al_{10.1}O_{17}$:$Cr^{3+}$ ($\lambda_{max} = 725$ nm, FWHM = 102 nm),[22] $ScBO_3$:Cr^{3+} ($\lambda_{max} = 774$ nm, FWHM = 120 nm),[23] and other materials exhibit varying luminescence characteristics. These findings suggest that the crystal field of the host matrix plays a significant role in determining the luminescence bandwidth of Cr^{3+} ions. The perovskite structure of ABO_3, as a luminescent matrix material, offers outstanding performance, featuring low phonon energy and stable chemical properties.

In this work, varying Cr^{3+}-doped $GaScO_3$ with ABO_3 perovskite structure have been synthesized with traditional high-temperature solid-state reaction method. The structural and luminescence properties of $GaScO_3$:Cr^{3+} were thoroughly investigated. Additionally, first-principles calculations were performed to reveal the band structure and mechanical properties of $GaScO_3$. Overall, $GaScO_3$:Cr^{3+} exhibits broad NIR emission with a full width at half maximum (FWHM) of 145 nm upon excitation at 465 nm, indicating its potential for wideband NIR emission applications.

2. Experimental details

2.1. Preparation of samples

Phosphor samples were prepared via conventional solid-state synthesis, employing the following protocol: (i) stoi-

†Corresponding author. E-mail: sjding@ahut.edu.cn

© 2025 Chinese Physical Society and IOP Publishing Ltd. All rights, including for text and data mining, AI training, and similar technologies, are reserved.

chiometric weighing of Sc_2O_3 (99.99%), Ga_2O_3 (99.9%), and Cr_2O_3 (99.9%) precursors; (ii) mechanical mixing (grind in an agate mortar crucible for 30 minutes) to achieve $x = 0.1$ at.%–5.0 at.% Cr^{3+} doping levels; (iii) high-temperature sintering (1500 °C, 12 h) in an ambient atmosphere; and (iv) controlled cooling to room temperature followed by final grinding for analytical characterization.

2.2. Characterizations

Comprehensive material characterization was conducted through multiple analytical platforms: x-ray diffraction (XRD) patterns were acquired (Bruker D8 Focus, Cu-$K\alpha$, 40 kV/40 mA) with refined structural analysis using VESTA. Vibrational properties were examined via Fourier transform infrared spectroscopy (FTIR) (Nicolet 6700) and Raman spectroscopy (Renishaw inVia). Morphological and compositional features were investigated using FE-SEM (Hitachi S-4800) with energy dispersive spectrometer (EDS) capability. Optical properties were characterized through diffuse reflectance (Shimadzu UV-3600) and photoluminescence spectroscopy (Edinburgh FLS-1000), including lifetime measurements at room temperature.

2.3. DFT calculation

Ab initio calculations were implemented using DFT-PAW (DFT: density functional theory, PAW: projector augmented wave) methodology with GGA-PBE (GGA: generalized gradient approximation, PBE: Perdew–Burke–Ernzerhof) exchange–correlation functional. Computational parameters were optimized through convergence tests: plane-wave cutoff energy (500 eV), k-point mesh ($7 \times 6 \times 7$, Monkhorst–Pack scheme), energy tolerance (10^{-6} eV), and force convergence (0.02 eV/Å). Structural optimization involved simultaneous relaxation of lattice vectors and atomic coordinates. Electronic structure analysis included charge density difference calculations, visualized through isosurface plots (0.005 e/Å^3) with cyan/yellow color coding for charge depletion/accumulation regions.

3. Results and discussion

3.1. Structure analysis

Phase analysis of GSO:Cr^{3+} phosphors (Fig. 1(a)) confirmed single-phase formation, indexed to the standard pattern (PDF#00-020-1034). The observed 2θ shift (Fig. 1(b)) follows Vegard's law, reflecting lattice contraction due to Ga^{3+} (0.62 Å) → Cr^{3+} (0.615 Å) substitution. Structural refinement (Fullprof Suite-2020) of the optimal composition (1.0-at.% Cr^{3+}, Fig. 1(c)) revealed an orthorhombic structure with refined parameters: $a = 5.74602$ Å, $b = 7.93123$ Å, and $c = 5.48272$ Å, demonstrating precise Cr^{3+} incorporation without secondary phase formation.

Figure 2(a) illustrates the Raman spectrum of GSO:Cr^{3+}, with the observed Raman shifts and their corresponding assignments summarized in Table 1. The shifts observed at the Cr_2O_3 (319.2 cm^{-1}) and Ga_2O_3 (643.9 cm^{-1}) peaks suggest the formation of a GSO compound that likely adopts a perovskite structure. Cation substitution within this structure leads to lattice distortion, which can result in phonon mode softening or hardening. The peaks at 532.6 cm^{-1}, 770.3 cm^{-1}, and 898.6 cm^{-1} correspond to specific vibrational modes. Vibrational spectroscopy revealed characteristic modes at 532.6 cm^{-1} and 770.3 cm^{-1}, corresponding to octahedral-site (Cr/Ga–O) vibrations.

Fourier-transform infrared (FT-IR) spectroscopy serves as a reliable analytical tool for determining phonon energy and elucidating structural characteristics of the samples.[24] The FT-IR spectra (3500 cm^{-1}–400 cm^{-1}) revealed three prominent absorption bands: (i) a broad band centered at 3447 cm^{-1} corresponding to O–H stretching vibrations of surface-adsorbed water molecules, (ii) a distinct peak at 1636 cm^{-1} attributed to H–O–H bending vibrations of molecular water, and (iii) two characteristic vibrational modes at 649 cm^{-1} and 582 cm^{-1} associated with Cr–O stretching vibrations in the crystal lattice. The FT-IR spectrum provides a reliable method for determining phonon energy and unveiling various structural details of samples.[25] The detailed analysis is shown in Table 1. Structural visualization (VESTA) confirmed

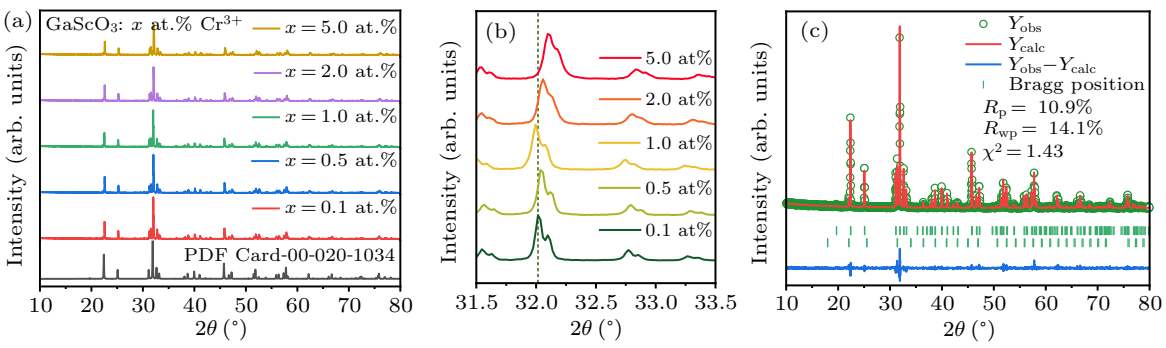


Fig. 1. (a) XRD patterns of $GaScO_3$: x at.% Cr^{3+} ($x = 0.1$, 0.5, 1.0, 2.0, and 5.0, respectively). (b) XRD patterns in 2θ in a range of 31.5°–33.5°. (c) Rietveld refinement results of $GaScO_3$:1.0-at.% Cr^{3+}.

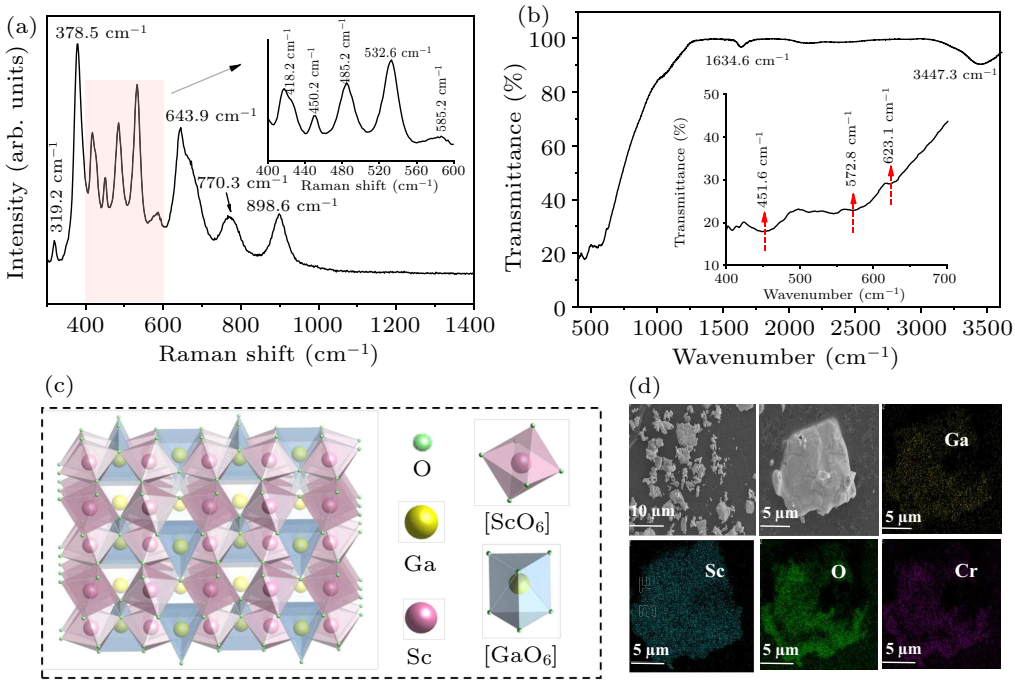


Fig. 2. (a) Raman spectrum of $GaScO_3$:Cr^{3+}, (b) FTIR spectra of the $GaScO_3$:Cr^{3+}, (c) unit cell structure of $GaScO_3$, (d) SEM photograph of $GaScO_3$:Cr^{3+} and element mapping under the selected region.

Table 1. Peak location and potential attribution.

Observed wavenumber (cm^{-1})	Possible attribution	References
319.2	A_{1g} mode of Cr_2O_3 (shifted)	[25]
378.5	Sc–O vibrations	[26]
418.2	symmetric Ga–O stretching (β-Ga_2O_3)	[27]
450.2	Sc–O vibrations in distorted lattice	[26]
485.2	Cr–O E_g mode (modified by Ga/Sc doping)	[25]
532.6	asymmetric M–O vibrations in spinel-type phase	
585.2	Cr–O E_g mode with lattice stiffening	[25]
643.9	Ga–O stretching in β-Ga_2O_3 (shifted)	[27]
770.3	tetrahedral M–O vibrations (spinel/defect modes)	
898.6	high-frequency M–O stretching in ordered phases	

cubic symmetry in the GSO perovskite framework (Fig. 2(c)). SEM-EDS mapping of GSO:5-at.% Cr^{3+} (Fig. 2(d)) demonstrated homogeneous elemental distribution (Ga, Sc, O, Cr), verifying successful Cr^{3+} incorporation into the host lattice.

3.2. DFT calculation of gallium scandium

Figure 3(a) presents the energy band structure of GSO in the first Brillouin zone. From the plot, it is evident that the doped GSO exhibits a direct bandgap with gap value of 4.06 eV. Band structure calculations confirm direct bandgap characteristics, enabling momentum-conserving interband transitions. The projected DOS (Fig. 3(b)) demonstrates orbital-specific contributions: Sc 3d orbitals exhibit pronounced peaks within ±2 eV of the Fermi level, indicating strong localization, while Ga 4p and O 2p orbitals dominate the conduction and valence band edges, respectively. This orbital decomposition elucidates the fundamental electronic properties governing optical transitions in GSO.

Figure 3(c) illustrates the electron density distribution of the highest occupied molecular orbitals (HOMO). The electron cloud is spatially localized in certain regions, indicating the areas with the highest probability of finding electrons. As the HOMO represents the highest-energy occupied molecular orbital, its electrons are the most reactive and are typically the first to participate in chemical interactions. Frontier molecular orbital theory indicates that the HOMO–LUMO (lowest unoccupied molecular orbital) energy gap critically determines electronic properties. In GSO, the HOMO (O 2p) → LUMO (Sc 3d) transition probability increases with decreasing energy separation, modifying electron density distribution. Orbital decomposition analysis (Fig. 3) reveals that the $[GaO_3]^{3-}$ groups dominate the electronic structure, governing both conductivity and chemical reactivity through their influence on frontier orbital energies.

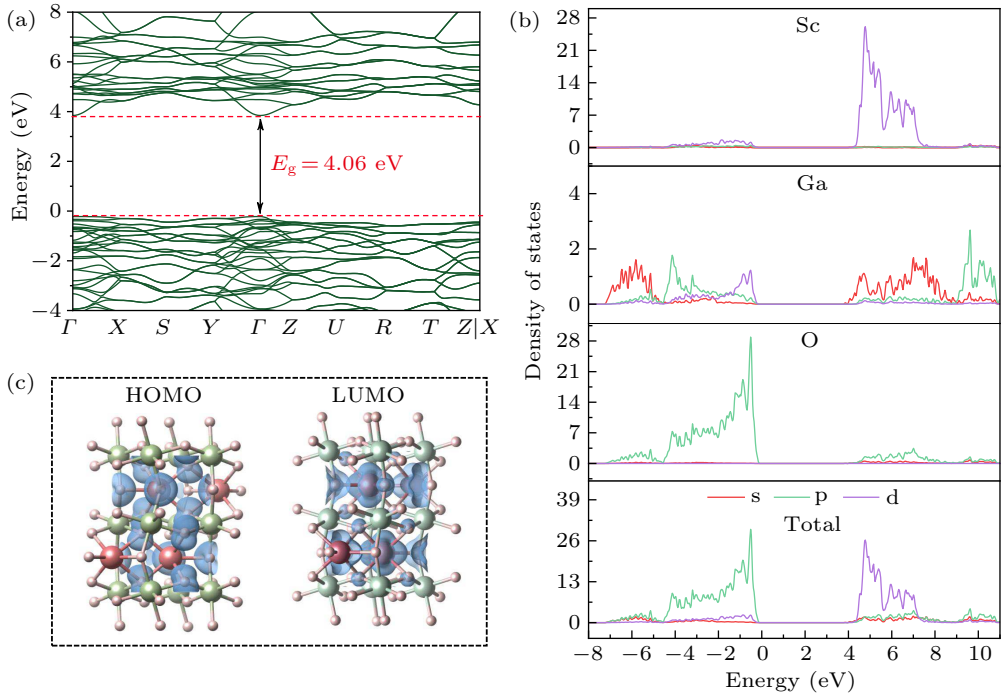


Fig. 3. (a) Band structure of $GaScO_3$. (b) The total DOS and partial DOS of $GaScO_3$. (c) The HOMO and LUMO orbitals of $GaScO_3$ are represented by the red ball for Sc atoms, and the pink and green balls for O and Ga atoms respectively.

3.3. Mechanical property analysis

The calculated elastic constants of GSO are presented in Table 2. Here, C_{ij} denotes the independent matrix element located at the intersection of row i and column j in the stiffness matrix. The GSO cubic crystal system exhibits high symmetry, and the relationship between its mechanical properties and elastic constants can be articulated as follows:[28]

$$B = \frac{C_{11} + 2C_{12}}{3}, \tag{1}$$

$$G_{\mathrm{R}} = \frac{5C_{44}(C_{11} - C_{12})}{4C_{44} + 3(C_{11} - C_{12})}, \tag{2}$$

$$G_{\mathrm{V}} = \frac{1}{5}(C_{11} - C_{12} + 3C_{44}), \tag{3}$$

$$G = \frac{G_{\mathrm{V}} + G_{\mathrm{R}}}{2}, \tag{4}$$

$$Y = \frac{9GB}{3B + G}, \tag{5}$$

$$\chi = \frac{3B - 2G}{2(3B + G)}. \tag{6}$$

Here, G_{V} represents the shear modulus calculated using the Voigt method, and G_{R} represents the shear modulus calculated using the Reuss method. Based on the elastic constants listed in Table 2, the mechanical properties of the GSO series materials were calculated using Eqs. (1)–(6), with the results presented in Table 3. The mechanical behavior of GSO was characterized through elastic moduli analysis. The B/G ratio of 3.35 significantly exceeds the brittle–ductile transition threshold (1.75), indicating inherent ductility.[29] Poisson's ratio ($\chi = 0.36$) further confirms this behavior, approaching the typical value for metallic systems (0.33) rather than covalent (0.15) or ionic (0.23) materials.[30] These parameters suggest metallic-like bonding characteristics in GSO, consistent with its electronic structure.

Table 2. Elastic constants for $GaScO_3$.

C_{11}	C_{12}	C_{13}	C_{21}	C_{22}	C_{23}	C_{31}	C_{32}	C_{33}	C_{44}	C_{55}	C_{66}
319.696	126.419	131.282	126.419	382.606	147.894	131.282	147.894	211.201	101.054	62.689	76.653

$$C_{11} > 0,\ C_{44} > 0,\ C_{11} > |C_{12}|,\ C_{11} - 2C_{12} > 0, \tag{7}$$

$$\begin{aligned} &C_{11} > 0,\ C_{22} > 0,\ C_{33} > 0,\ C_{44} > 0,\\ &C_{55} > 0,\ C_{66} > 0,\ (C_{33}C_{55} - C_{35}^2) > 0,\\ &(C_{44}C_{66} - C_{46}^2) > 0,\ (C_{22} + C_{33} - 2C_{23}) > 0,\\ &[C_{11} + C_{22} + C_{33} + 2(C_{12} + C_{13} + C_{23})] > 0. \end{aligned} \tag{8}$$

By substituting the elastic constants of GSO in Table 2 into Eqs. (7) and (8), the above stability criteria are satisfied, indicating that this series of materials can exist in a stable structure of cubic and monoclinic. Three-dimensional elastic property visualization (Fig. 4) reveals anisotropic mechanical behavior in cubic GSO: (i) Young's modulus (E) maximizes along the [001] and [010] directions; (ii) shear modulus (G) and Poisson's ratio (χ) peak in the [111] direction. This directional dependence reflects the cubic system's high symmetry, with maximum stiffness along the principal axes and enhanced

shear resistance along the body diagonal.

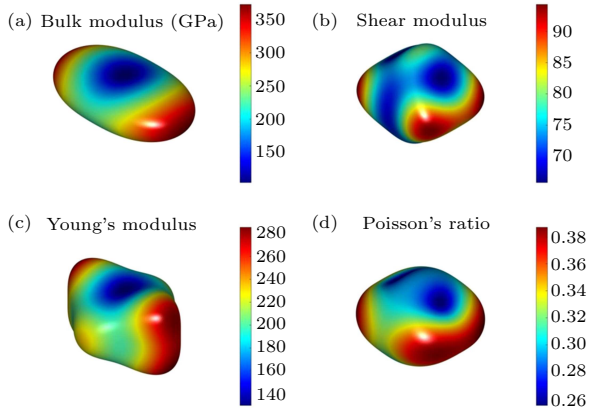


Fig. 4. (a) Bulk modulus, (b) shear modulus, (c) Young's modulus, and (d) Poisson's ratio of $GaScO_3$ in three dimensions.

Table 3. Mechanical properties of $GaScO_3$.

Y (GPa)	B (GPa)	G (GPa)	χ
303.469	372.550	111.223	0.36

Optical properties are quantitatively described by the complex dielectric function $\varepsilon(\omega)$, comprising real (ε_1) and imaginary (ε_2) components that respectively govern energy storage and dissipation. These frequency-dependent parameters are fundamentally connected to the material's electronic structure through dipole transition matrix elements and joint density of states.[3] Optical parameters such as the refractive index $n(\omega)$, reflectance $R(\omega)$, absorption coefficient $\alpha(\omega)$, and extinction coefficient $k(\omega)$ are related to the dielectric function as follows:[31,32]

$$n(\omega) = \frac{1}{\sqrt{2}}\left(\sqrt{\varepsilon_1^2(\omega)+\varepsilon_2^2(\omega)}+\varepsilon_1(\omega)\right)^{1/2}, \tag{9}$$

$$R(\omega) = \left|\frac{\sqrt{\varepsilon(\omega)}-1}{\sqrt{\varepsilon(\omega)}+1}\right|^2, \tag{10}$$

$$\alpha(\omega) = \sqrt{2}\omega\left(\sqrt{\varepsilon_1^2(\omega)+\varepsilon_2^2(\omega)}-\varepsilon_1(\omega)\right)^{1/2}, \tag{11}$$

$$k(\omega) = \frac{1}{\sqrt{2}}\left(\sqrt{\varepsilon_1^2(\omega)+\varepsilon_2^2(\omega)}-\varepsilon_1(\omega)\right)^{1/2}. \tag{12}$$

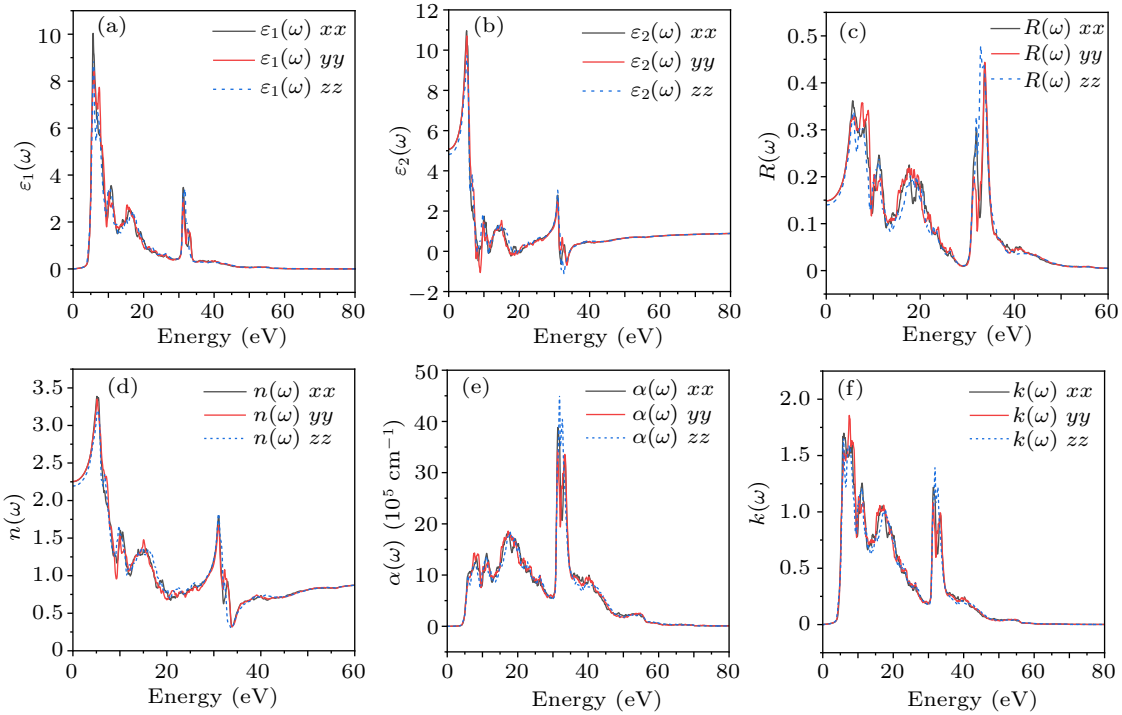


Fig. 5. The calculated (a) real part and (b) imaginary part, (c) reflectance $R(\omega)$, (d) refractive index $n(\omega)$, (e) absorption coefficient $\alpha(\omega)$, (f) extinction coefficient $k(\omega)$ of $GaScO_3$.

The optical properties of GSO, calculated using first-principles methods, are shown in Fig. 5. The static values of the real part $\varepsilon_1(\omega)$ of the dielectric function at zero frequency $(\varepsilon_1(\omega), \omega = 0)$ are calculated to be $\varepsilon_1^{xx}(0) = 5.07$, $\varepsilon_1^{yy}(0) = 5.05$, and $\varepsilon_1^{zz}(0) = 4.81$. As shown in Fig. 5(a), the real part $\varepsilon_1(\omega)$ increases rapidly with photon energy from its initial value, reaching a maximum of approximately 4.99 eV. As photon energy continues to increase, $\varepsilon_1(\omega)$ exhibits a monotonically decreasing trend, reaching a minimum value near 8.91 eV. Between 8.91 eV and 33.50 eV, $\varepsilon_1(\omega)$ shows a non-monotonic variation, after which it increases monotonically again, approaching a value of 1.0 as the photon energy approaches 80 eV. Overall, the $\varepsilon_1(\omega)$ function demonstrates high isotropy across the entire energy range, with the three components $\varepsilon_1^{xx}(\omega)$, $\varepsilon_1^{yy}(\omega)$, and $\varepsilon_1^{zz}(\omega)$ being nearly identical. When the photon energy falls within the ranges of 7.78 eV–9.37 eV, 17.20 eV–19.86 eV, and 31.41 eV–34.46 eV, the $\varepsilon_1(\omega)$ function becomes negative, indicating that the GSO exhibits metal-like or plasma-like properties. Optical characterization reveals distinct spectral features: (i) $\varepsilon_2(\omega)$ exhibits

a sharp onset at 3.044 eV, peaking at 5.682 eV (Fig. 5(b)); (ii) reflectivity $R(\omega)$ shows static values of $R^{xx}(\omega) = 14.90\%$, $R^{yy}(\omega) = 14.88\%$, $R^{zz}(\omega) = 13.95\%$, with maximum reflectivity (44.33%) at 33.351 eV (Fig. 5(c)); (iii) high reflectivity ($> 30\%$) occurs in two spectral windows (5.14 eV–9.34 eV and 32.37 eV–34.27 eV); (iv) static refractive indices are $n^{xx}(\omega) = 2.25$, $n^{yy}(\omega) = 2.24$, $n^{zz}(\omega) = 2.20$ (Fig. 5(d)). Combining this with Fig. 5(a), it is evident that the real part $\varepsilon_1(\omega)$ of the complex dielectric function closely resembles the refractive index, mainly because the following equation is strictly satisfied between the complex dielectric function and the complex refractive index:[33]

$$\varepsilon = (n + \mathrm{i}k)^2. \tag{13}$$

Here, ε represents the complex dielectric function, n denotes the refractive index, k is the extinction coefficient, and i is the imaginary unit. Simplifying the equations yields $\varepsilon_1 = n^2 - k^2$ and $\varepsilon_2 = 2nk$. The complex dielectric function components exhibit distinct physical origins: $\varepsilon_1(\omega)$ primarily reflects the refractive index $n(\omega)$, while $\varepsilon_2(\omega)$ is proportional to $n(\omega)k(\omega)$. Optical absorption analysis reveals the following: (i) an absorption onset at 4.12 eV with nonlinear energy dependence; (ii) a maximum absorption coefficient $\alpha_{max} = 43 \times 10^5$ cm^{-1} at 31.87 eV (Fig. 5(e)). The extinction coefficient $k(\omega)$ (Fig. 5(f)) demonstrates strong correlation with $\varepsilon_2(\omega)$, particularly in peak positions and spectral profiles, reflecting consistent light–matter interaction mechanisms.[6]

3.4. Absorption properties of gallium scandium

The diffuse reflectance (DR) spectra of GSO:xCr^{3+} phosphors were measured to investigate their light absorption properties. The results are shown in Fig. 6(a). The Cr^{3+}-doped samples exhibit strong absorption in the 400 nm–500 nm and 600 nm–700 nm regions of the visible spectrum, corresponding to the $^4A_2 \rightarrow {}^4T_1$ and $^4A_2 \rightarrow {}^4T_2$ electronic transitions of Cr^{3+}, respectively.[34] The photoluminescence excitation (PLE) and photoluminescence (PL) spectra for GSO:2-at.% Cr^{3+} are shown in Fig. 6(b). The PLE spectrum displays two broad bands in the blue and red regions, which align well with the DR spectral results. Upon excitation at 465 nm, an NIR emission band centered at 774 nm is observed for GSO:1-at.% Cr^{3+}, corresponding to the $^4T_2 \rightarrow {}^4A_2$ transition of Cr^{3+}. Figure 6(c) denotes the energy level transition diagram of Cr^{3+} according to the PLE and PL spectra. Bandgap analysis based on Tauc plots revealed direct allowed transitions ($n = 1/2$) in GSO, following[35,36]

$$[h\nu\alpha]^{1/n} = A\left(h\nu - E_g\right), \tag{14}$$

where α, $h\nu$, and A denote the absorption coefficient, photon energy, and material constant, respectively. Cr^{3+} incorporation (0.1 at.%–5.0 at.%) systematically modulated the bandgap (3.43 eV–3.74 eV, Fig. 6(e)) through lattice distortion effects. Optical characterization of GSO:1-at.% Cr^{3+} yielded a broad emission band (FWHM = 145 nm, Fig. 6(f)), with the spectral width exceeding that of most reported Cr^{3+}-activated phosphors, indicating superior performance for NIR light sources.

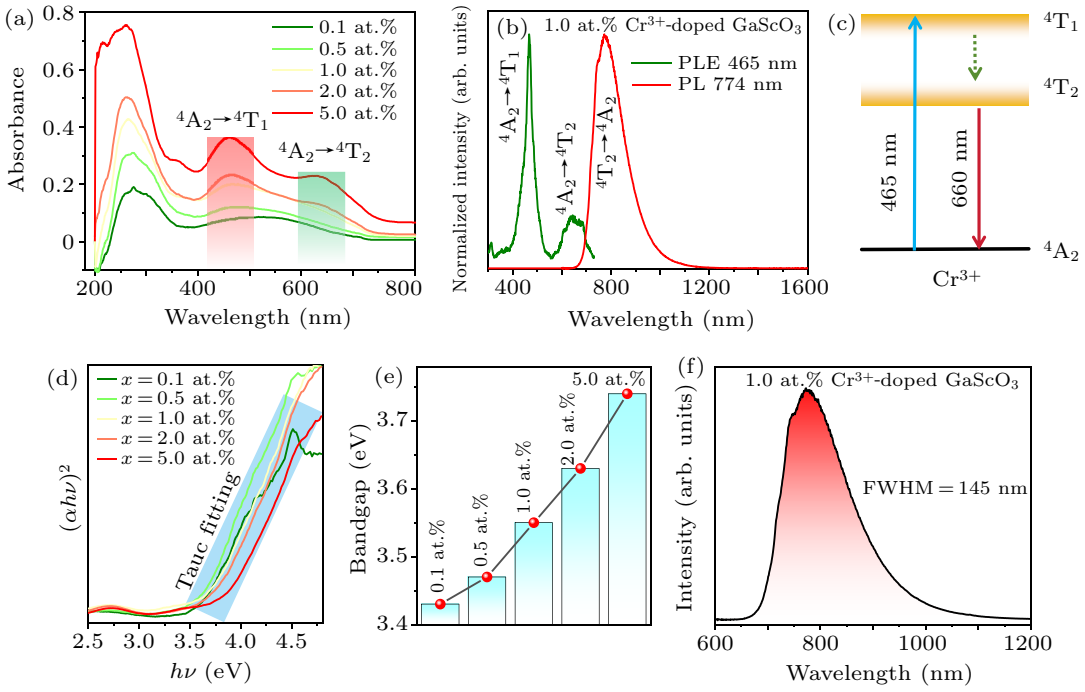


Fig. 6. (a) The diffuse reflectance spectra of GaScO$_3$:x-at.% Cr^{3+} ($x = 0.1$, 0.5, 1.0, 2.0, 5.0). (b) Emission and excitation spectra of GaScO$_3$:1-at.% Cr^{3+}. (c) Energy level transition diagram of Cr^{3+}. (d) The plot of $(\alpha h\nu)^2$ versus $h\nu$ for GaScO$_3$:x-at.% Cr^{3+}. (e) The variation trend of the bandgap width in GaScO$_3$:x-at.% Cr^{3+}. (f) The FWHM of GaScO$_3$:1-at.% Cr^{3+}.

Table 4. The comparison of photoluminescence (PL) properties between Cr^{3+}:GSO and typical Cr^{3+}-doped NIR emitting phosphors.

Samples	Excitation (nm)	Peak position (nm)	FWHM (nm)	Dq/B	Ref.
Cr^{3+}:$GaScO_3$	465	774	145	2.2	this work
Cr^{3+}:$GaTaO_4$	470	825	127	2.29	[34]
Cr^{3+}:$CaLu_2Mg_3O_{12}$	450	765	120	2.17	[37]
Cr^{3+}:$Ga_{0.5}Ta_{0.5}O_4$	474	836	137	2.07	[4,38]
Cr^{3+}:$ScTa_{0.5}Nb_{0.5}O_4$	430	970	192	2.18	[36]

3.5. Photoluminescence properties of gallium scandium

Photoluminescence analysis of GSO:x-at.% Cr^{3+} crystals ($x = 0.1$–5.0) revealed concentration-dependent emission characteristics (Figs. 7(a) and 7(b)). The emission intensity followed a non-monotonic trend, reaching the maximum luminous intensity at $x = 1$ at.% before exhibiting concentration quenching due to enhanced non-radiative recombination via Cr^{3+}–Cr^{3+} energy transfer. The emission profile's sensitivity to local coordination geometry stems from crystal field splitting of Cr^{3+}'s 3d orbitals, with the $^4T_2 \rightarrow {}^4A_2$ transition energy varying according to the ligand field strength. The "T–S diagram," devised by Yukito Tanabe and Satoru Sugano, was developed to explain the inter-electronic transitions within d-orbitals for the $3d^n$ configuration (where n ranges from 2 to 8). Figure 7(c) presents the T-diagram for the $3d^3$ configuration of Cr^{3+} ions in octahedral lattice sites.[39] The value of Dq/B is generally calculated using the following equations:[40]

$$10Dq = E(^4T_2) = E(^4A_2 \rightarrow {}^4T_2) - \Delta S/2, \quad (15)$$

$$\Delta S = E(^4A_2 - {}^4T_2) - E(^4T_2 - {}^4A_2), \quad (16)$$

$$Dq/B = [15(a-8)/(a^2-10a)], \quad (17)$$

$$a = [E(^4A_2 \rightarrow {}^4T_1) - E(^4A_2 \rightarrow {}^4T_2)]/Dq. \quad (18)$$

Here, ΔS represents the Stokes shift and is used to ensure the accuracy of $E(^4T_2)$. The transition energies, $E(^4A_2 \rightarrow {}^4T_2)$, $E(^4A_2 \rightarrow {}^4T_1)$, and $E(^4T_2 \rightarrow {}^4A_2)$, are calculated using the excitation and emission peaks from the excitation and emission spectra. The Dq/B values for GSO doped with 2%- and 5%-Cr^{3+} are calculated to be 2.2 and 2.13, respectively. The detailed calculation data are presented in Table 4. The relatively weaker crystal field allows the Cr^{3+}-doped GSO phosphor to exhibit wide-band NIR emission.[34] In addition, the reduction in Dq/B can be attributed to the smaller ionic radius of Cr^{3+}, which induces lattice shrinkage and a consequent decrease in crystal field intensity.[41] As a result, this leads to a redshift of the emission peak, as shown in Fig. 7(b). Figure 7(d) illustrates the fluorescence attenuation curve of GSO doped with 1 at.% at 774 nm under 465-nm excitation. This decay curve can be accurately fitted using a single exponential function[42]

$$I(t) = I_0 \exp(-t/\tau), \quad (19)$$

where $I(t)$ denotes the luminescent intensity at time t, I represents the background intensity, and τ signifies the lifetime. The final fitting result is approximately 112.47 μs.

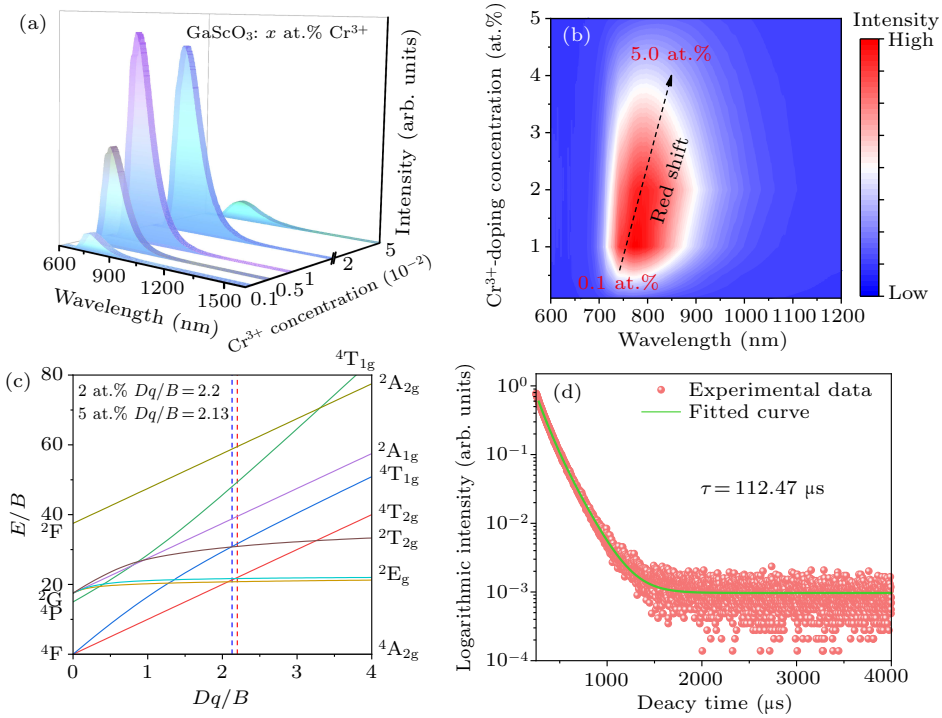


Fig. 7. (a) and (b) PL spectra of $GaScO_3$:x-at.% Cr^{3+} ($x = 0.1$, 0.5, 1.0, 2.0, 5.0). (c) The Tanabe–Sugano diagram of 2-at.% and 5-at.% $GaScO_3$:Cr^{3+}. (d) The luminescent decay curves of $GaScO_3$: 1-at.% Cr^{3+} at room temperature.

Table 5. Estimated crystal field parameters of the $GaScO_3$:Cr^{3+} with doping concentrations of 2 at.% and 5 at.%, respectively.

Concentration	$10Dq$ (cm^{-1})	B (cm^{-1})	Dq/B	a
2 at.%	10913.6	496.1	2.2	4.39
5 at.%	10728.5	503.7	2.13	4.48

4. Conclusions

In summary, a series of Cr^{3+}-activated GSO phosphors have been synthesized for promising NIR emission applications. The structure of the synthesized GSO:Cr^{3+} phosphors was investigated and confirmed to exhibit a perovskite structure. Upon excitation at 465 nm, the phosphors demonstrate remarkable broadband NIR emission spanning the range of 700 nm–1200 nm, with FWHM of approximately 145 nm. Additionally, the optical properties, elastic modulus, and dielectric constant of GSO were calculated using first-principles methods. Overall, the results suggest that perovskite GSO:Cr^{3+} phosphors hold significant potential for wide-band NIR pc-LED applications.

Acknowledgements

Project supported by the Natural Science Research Project of Anhui Provincial Education Department for Excellent Young Scholars (Grant No. 2024AH030007) and the National Natural Science Foundation of China (Grant No. 52202001).

References

[1] Yu D C, Ding Q Y, Shen T T, Qiu L, He F Q, Han X X, Song E H, Zhuang S L and Zhang D W 2024 *Dalton Trans.* **53** 3702
[2] Ding Q Y, Wu J C, Yu D C, Han X X, Zhou Y Y, Shen T T, Ma Y F, Zhuang S L and Zhang D W 2024 *J. Mater. Chem. C* **12** 2184
[3] Zhuo M P, Wang X D and Liao L S 2022 *Small Sci.* **2** 2200029
[4] Lou L L, Zhao S, Yuan S W, Zhu D Y, Wu F G and Mu Z F 2022 *Inorg. Chem. Front.* **9** 3522
[5] Ding S J, Ren H, Liu W P, He A F, Tang X B and Zhang Q L 2022 *CrystEngComm.* **24** 818
[6] Huang H, Li R F, Jin S L, Li Z F, Huang P, Hong J Q, Du S W, Zheng W, Chen X Y and Chen D Q 2021 *ACS Appl. Mater. Interfaces* **13** 34561
[7] Yu D C, Zhou Y S, Ma C S, Melman J H, Baroudi K M, LaCapra M and Riman R E 2019 *ACS Appl. Electron. Mater.* **1** 2325
[8] Jin S Y and Xu X S 2024 *Chin. Phys. B* **33** 036102
[9] Zhang Q Q, Liu D J, Wang Z N, Dang P P, Lian H Z, Li G G and Lin J 2023 *Adv. Opt. Mater.* **11** 2202478
[10] Liang S S, Shang M M, Lian H Z, Li K, Zhang Y and Lin J 2016 *J. Mater. Chem. C* **4** 6409
[11] He S, Zhang L L, Wu H, Wu H J, Pan G H, Hao Z D, Zhang X, Zhang L G, Zhang H and Zhang J H 2020 *Adv. Opt. Mater.* **8** 1901684
[12] Botella P, Enrichi F, Vomiero A, Munoz-Santiuste J E, Garg A B, Arvind A, Manjon F J, Segura A and Errandonea D 2020 *ACS Omega.* **5** 2148
[13] Saikia S, Ghosh A and Nag A 2023 *Angew. Chem. Int. Ed. Engl.* **62** e202307689
[14] Li J H, Zhang Q L, Sun G H, Gao J Y, Dou R Q, Wang X F and Ding S J 2024 *Chin. Phys. B* **33** 117601
[15] Qiao J W, Zhou G J, Zhou Y Y, Zhang Q Y and Xia Z G 2019 *Nat. Commun.* **10** 5267
[16] Zabiliute A, Butkute S, Zukauskas A, Vitta P and Kareiva A 2014 *Appl. Opt.* **53** 907
[17] Zhu F M, Gao Y, Zhu B M, Huang L and Qiu Ji B 2024 *Chem. Eng. J.* **479** 147568
[18] Liu G C, Molokeev Maxim S, Lei B F and Xia Z G 2020 *J. Mater. Chem. C* **8** 9322
[19] Mao M Q, Zhou T L, Zeng H T, Wang L, Huang F, Tang X Y and Xie R J 2020 *J. Mater. Chem. C* **8** 1981
[20] Wang C P, Wang X M, Zhou Y, Zhang S, Li C, Hu D F, Xu L and Jiao H 2019 *ACS Appl. Electron. Mater.* **1** 1046
[21] Lin Q M, Wang Q, Liao M, Xiong M X, Feng X, Zhang X, Dong H F, Zhu D Y, Wu F G and Mu Z F 2021 *ACS Appl. Mater. Interfaces* **13** 18274
[22] Zheng L W, Kuang J L, Shen J X, Wu H J, Wu H, Luo Y S, Pan G H, Hao Z D, Zhang L L and Zhang J H 2023 *ACS Appl. Opt. Mater.* **1** 1150
[23] Fang M H, Huang P Y, Bao Z, Majewska Natalia, Leśniewski Tadeusz, Mahlik Sebastian, Grinberg Marek, Leniec Grzegorz, Kaczmarek Slawomir M, Yang C W, Lu K M, Sheu H S and Liu R S 2020 *Chem. Mater.* **32** 2166
[24] Zhang C C, Ding S J, Wang M M, Ren H, Tang X B, Zou Y, Dou R Q and Liu W P 2023 *Front. Optoelectron.* **16** 31
[25] Attah-Baah J M, Santos C, Silva R S, Oliveira J L, Jucá R F, Costa B F O, Matos R S, Escote M T, Silva R S, Rezende M V S and Ferreira N S 2024 *Ceram. Int.* **50** 35714
[26] de Jesus Pereira A L, Sans J A, Vilaplana R, Ray S, Tadge P, Godoy A, Horta I M, da Silva-Sobrinho A S, Rodríguez-Hernández P, Muñoz A, Popescu C and Manjón F J 2024 *Minerals* **15** 21
[27] Yao R C, Wan L Y, Li B S and Wang Y F 2024 *Appl. Phys. Express* **17** 012004
[28] Pugh S F 2009 *Philos. Mag.* **45** 823
[29] Born Max 2008 *Math. Proc. Cambridge Philos. Soc.* **36** 160
[30] Dar Sajad A, Khandy Shakeel A, Islam I, Gupta D C, Sakalle U K, Srivastava V and Parrey K 2017 *Chin. J. Phys.* **55** 1769
[31] Mubashir S, Butt Mehwish K, Yaseen M, Iqbal J, Iqbal M, Murtaza A and Laref A 2021 *Optik* **239** 166694
[32] Gassoumi A and Saad H E M M 2016 *Mater. Sci. Semicond. Process.* **50** 14
[33] Behram Rasul B, Iqbal M A, Alay-e-Abbas S M, Sajjad M, Yaseen M, Arshad M I and Murtaza G 2016 *Mater. Sci. Semicond. Process.* **41** 297
[34] Zhong J Y, Zhuo Y, Du F, Zhang H S, Zhao W R, You S H and Brgoch Jakoah 2021 *Adv. Opt. Mater.* **10** 2101800
[35] Makula P, Pacia M and Macyk W 2018 *J. Phys. Chem. Lett.* **9** 6814
[36] Ding S J, Li C, Zhang M Y, Zhang C C, Hu H T, Zou Y, Tang X B and Liu W P 2025 *J. Alloys Compd.* **1014** 178571
[37] Li R Y, Liu Y F, Yuan C X, Leniec Grzegorz, Miao L J, Sun P, Liu Z H, Luo Z H, Dong R and Jiang J 2021 *Adv. Opt. Mater.* **9** 2100388
[38] Liu S B, Wang G L, Xu L Y, Jia H X, Sun X K and Yuan H L 2023 *Ceram. Int.* **49** 33401
[39] Tanabe Y and Sugano S 1954 *J. Phys. Soc. Jpn.* **9** 766
[40] Yang Y, Lu Z Z, Fan H, Chen M H, Shen L W, Zhang X G, Pang Q, Chen J H, Chen P C and Zhou L Y 2023 *Inorg. Chem.* **62** 3601
[41] Zhang Q Q, Liu D J, Dang P P, Lian H Z, Li G G and Lin J 2021 *Laser Photon. Rev.* **16** 2100459
[42] Zhang Y, Miao S H, Liang Y J, Liang C, Chen D X, Shan X H, Sun K N and Wang X J 2022 *Light Sci. Appl.* **11** 136